



Cell degradation in commercial LiFePO_4 cells with high-power and high-energy designs



Matthieu Dubarry, Cyril Truchot, Bor Yann Liaw*

Electrochemical Power Systems Laboratory, Hawaii Natural Energy Institute, School of Ocean and Earth Science and Technology, University of Hawaii at Manoa, 1680 East-West Road, POST Bldg. 109, Honolulu, HI 96822, USA

HIGHLIGHTS

- Quantitative analyses of degradation modes in high-energy and high-power LiFePO_4 cells.
- High-power cells show rate-independent capacity fade due to loss of Li inventory (LLI).
- High-energy cells show rate-dependent fades from LLI and loss of active materials.
- Detailed dQ/dV analysis and simulation can reveal the attributing degradation modes.
- Electrochemical milling induces rate-dependent capacity increases in early cycle aging.

ARTICLE INFO

Article history:

Received 27 November 2013

Received in revised form

11 February 2014

Accepted 13 February 2014

Available online 22 February 2014

Keywords:

Degradation modes

Aging mechanism

Lithium iron phosphate

Capacity fade

Model simulation

dQ/dV analysis

ABSTRACT

A quantitative analysis is presented to determine the degradation modes attributing to capacity fade in commercial LiFePO_4 cells with high-power (HP) and high-energy (HE) designs. The capacity fade in the HP cell is predominantly due to the loss of lithium inventory. The fade in the HE cell is much more complicated as a function of rate. Using techniques including rest-cell-voltage measurements to track state-of-charge, dQ/dV analysis to trace peak area variations, and mechanistic model simulations (by the 'Alawa toolbox'), the capacity fades in the initial 120 cycles and subsequent aging are analyzed and degradation modes identified. Detailed 'Alawa' simulation with careful experimental validation explains the complexity of degradation in the HE cell. Peculiar rate-dependent initial capacity increases at rates higher than C/5 was likely attributed to electrochemical milling, resulting in active surface area increases and reduced polarization resistance (as the actual current density in the positive electrode was reduced). The mechanistic model and simulation capability illustrates the merits of this unique diagnostic approach with unprecedented holistic quantitative resolution for complicated cell degradation that seems hardly resolvable by other diagnostic methods.

© 2014 Elsevier B.V. All rights reserved.

1. Introduction

In recent years, several studies [1–9] have been published regarding the degradation of a number of commercial graphite|| LiFePO_4 (LFP) cells. Majority of the reports agree on a two-stage process of degradation, starting with loss of lithium inventory (LLI), followed by a combination of LLI, loss of active material (LAM), and reaction kinetics degradation (RKD). In our previous study on a commercial high-energy (HE) graphite||LFP cell [9], a peculiar rate-dependent capacity fading behavior was observed in the first 80 cycles of aging. Although the capacity fade was observed at lower

rates, the capacity was retained well at higher rates. The rest cell voltage (RCV) measured at the end-of-discharge (EOD) decreases with cycle number at all rates, suggesting that the cell was consistently being discharged to a lower state-of-charge (SOC) in these conditions. We speculated that this behavior was the result of a combination of LLI and a "reservoir effect" arisen from the loading matching between the positive electrode (PE) and negative electrode (NE) due to the cell design. As the rate increases in the discharge regime, a portion of the PE active materials (PEAM) was not fully utilized; thus, some of the Li content in the NE becomes available as a "Li reservoir" which compensates the LLI for higher rates and subsequent events. This hypothesis was later studied by a model simulation, which 'synthesized' this scenario successfully, as reported in Ref. [10]. Here we conducted additional tests with two different cell designs, high-power (HP) and HE, to provide

* Corresponding author. Tel.: +1 808 956 2339; fax: +1 808 956 2336.

E-mail addresses: boryann.liaw@gmail.com, Bliaw@hawaii.edu (B.Y. Liaw).

Table 1

Acronyms and nomenclatures.

BOD	Beginning-of-discharge
C/n	Rate in a test regime to discharge the rated capacity in 'n' hours
EOD	End-of-discharge
GIC	Graphite intercalation compounds
HE	High-energy (cell or design)
HP	High-power (cell or design)
IC	Incremental capacity or dQ/dV
LAM	Loss of active materials
LFP	Lithium iron phosphate with a nominal composition of LiFePO_4
LLI	Loss of lithium inventory
LR	Loading ratio ($Q_{\text{NE}}/Q_{\text{PE}}$)
NE	Negative electrode
NEAM	Negative electrode active material
PE	Positive electrode
PEAM	Positive electrode active material
$ps\text{-OCV}$	OCV Pseudo-open circuit voltage
OFS	Offset between electrode loadings introduced by the initial SEI formation and subsequent aging and degradation
Q	Capacity in general, also for the full cell and rated capacity when appropriate
RCV	Rest cell voltage
RKD	Reaction kinetics degradation
RPT	Reference performance test
SEI	Solid electrolyte interphase
SOC	State-of-charge
V_{IR}	Cell voltage immediately after the initial IR drop

experimental evidence to further validate the hypothesis, which suggests that the HE design should be the only one to exhibit such a behavior. By tracking the capacity and RCV evolutions at a variety of rates, from C/25 to 2 C, during the initial stage of cycle aging in the two cell designs, this unique capacity-fading phenomenon was investigated. Also investigated is a phenomenon peculiar in some LFP cells where capacity increases at high rates during the initial stage of cycle aging [11,12]. Whether the two phenomena were related was also studied in this work. The results suggest that the charge transfer rate appears improved in the cells that show increasing capacity with discharging rate, as suggested by the cell ohmic resistance derived from the initial IR drop upon polarization, which decreases as the cycle aging progresses. This behavior could be explained as a result of 'electrochemical milling' that occurs to the LFP grains in the PE, as suggested in Ref. [13] and by others who reported the observations of cracking LFP grains in the PE [14,15].

2. Experimental

Two batches of commercial graphite||LFP 26650 cylindrical cells from the same manufacturer were provided for the testing in this work. These cells are different from those used in Ref. [9] provided by another manufacturer. The cells of an HP design are rated 2.6 Ah and tested using a Maccor 4300 tester. The cells of an HE design are rated 3.2 Ah and tested using an Arbin BT-2043 tester. The HE cells use the Phostech PA LFP materials (of which the grains are typically 2–4 μm particles) [16], and the HP cells use Phostech P2 (in this case, the particle size is 0.5–1 μm) [17] in the PE. Graphite and its intercalation compounds (GIC) as the NE active material (NEAM) are assumed similar in both designs.

In our previous study [9], the cells were aged for 80 cycles with the 'dynamic stress test' schedule before commencing a reference performance test (RPT). With that test protocol, no suitable rate-dependent data was available to derive quantitative information on cycle aging behavior for detailed analyses of the initial 80 cycles. To rectify this drawback, a new protocol was implemented in this study, comprising a sequence of repetitive C/25, C/5, C/2, 1 C and 2 C constant current (CC) discharge regimes to a 2.5 V cutoff voltage in order to collect data on capacity variations in the course of cycle

aging to facilitate the analysis of rate-dependent fading behavior. All cells were recharged with a schedule recommended by the manufacturer, which comprises a C/2 CC charging step to 3.65 V followed by a constant voltage (CV) step until a cutoff current of C/25 is reached. At the EOD of each discharge regime, a 3-h rest was staged to track the evolution of RCV as a function of cycle number and rate. One cell from each design was arbitrarily chosen for determining the *pseudo*-open circuit voltage versus SOC ($ps\text{-OCV} = f(\text{SOC})$) curve for each design. The $ps\text{-OCV} = f(\text{SOC})$ curve was derived by averaging the voltage in the C/25 charge and discharge regime as a function of SOC, as explained in Refs. [9,18]. By a convention described in Ref. [19], the SOC is defined as the percentage of the residual capacity in the cell against the maximum capacity. Both residual and the maximum capacity should be determined with a sufficiently low rate such as C/25 to extract the charge without any residual remaining in the cell. The $ps\text{-OCV} = f(\text{SOC})$ curve was used to determine the SOC based on RCV in order to track the SOC variations as a function of rate and the extent of capacity fading in the aging process to characterize the performance of the cell accurately.

During the execution of the cycle aging of the HE cell, the Arbin channel data acquisition encountered a malfunction which introduced noisy data to the first 150 cycles, followed by a glitch from cycle 150 to 200 within which the capacity was not recorded properly. The test was resumed after the channel was repaired and recalibrated. Based on the RCV data salvaged in this period, no suspicious or peculiar effects were found from the test results, which ease our concern of possible artifacts that might compromise our tests and analyses.

Computer simulations were performed using a proprietary toolbox named 'Alawa', which is developed in our laboratory to serve as a user interface to facilitate the use of the model described in Ref. [10]. The model implemented in 'Alawa' includes some improvements in functionality and capability with additional inputs to allow users visualize the results from simulation. Some experimental validation supporting our simulation results based on LLI and LAM fading modes has been reported recently by other groups [20,21]. The simulation was performed using half-cell data; the LFP half-cell data was provided by Hydro-Quebec, and the data for GIC from TIMCAL. The results of the half-cell data were reported in Fig. 2 of Ref. [10]. Even though the relevant materials used in generating the half-cell data might not be the same as those used in the test cells, the trends derived from the simulation are quantitatively similar to the test results. Therefore, we are confident that

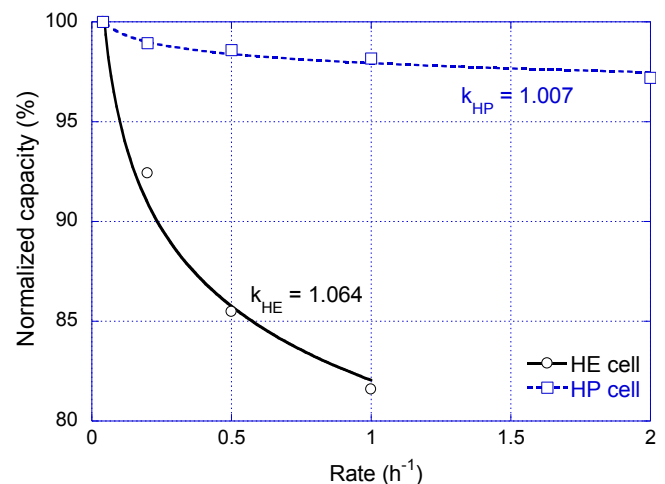


Fig. 1. Peukert curves for the HE (circles) and HP (squares) cells on a normalized capacity scale.

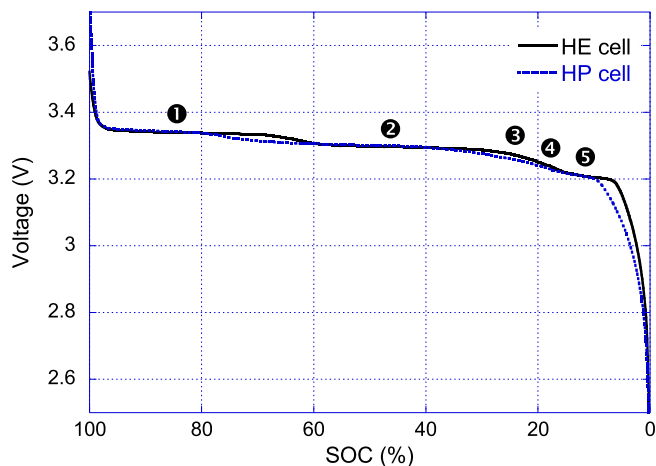


Fig. 2. The $ps\text{-OCV} = f(\text{SOC})$ curves for the HE (solid line) and HP (dotted line) cells.

the results derived from both experiments and simulations are relevant, and they should provide sufficient fidelity to explain the phenomena in this analysis. The similarity in the fading results between the HE cells used in this work and in Ref. [9] made by a different manufacturer supports the assertion that LFP does not play a significant role in determining the fading behavior.

3. Results

3.1. Rate capability

Fig. 1 shows the Peukert plots to exhibit the rate capability of the two types of cells on a normalized capacity scale. With the same form factor (i.e. 26650 size), the HP type shows a lower rated capacity but superior rate capability than the HE cell. For instance, the capacity is compromised by merely 2% from C/25 to 1C with the HP type, in contrast to 18% with the HE type. Both types follow the Peukert law, $Q = I^k t$, where t is the duration of the discharge regime

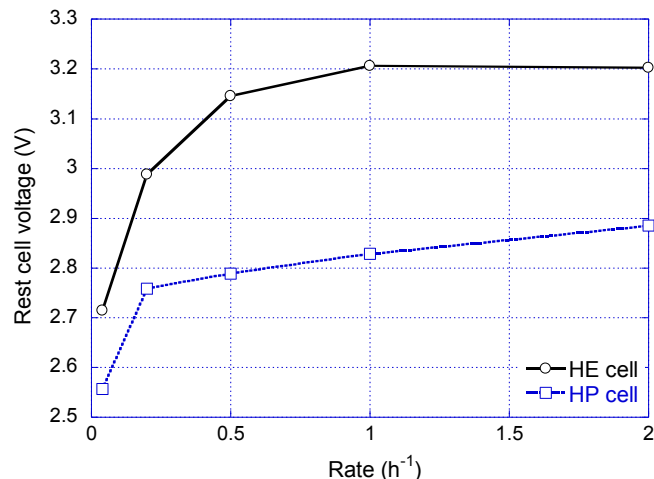


Fig. 3. The EOD rest cell voltage (RCV) as a function of discharge C rate for the HE (circles) and HP (squares) cells.

in hours, I the current, and k the Peukert coefficient. The rate capability comparison also reflected in the Peukert coefficient k ; i.e. $k_{\text{HE}} = 1.064$ and $k_{\text{HP}} = 1.007$, respectively. The ohmic resistance was estimated from the dependence of the IR-induced voltage drop (i.e. IR drop) at the beginning-of-discharge (BOD) as a function of rate, as discussed in Ref. [22] (data not shown). The ohmic resistance is on the order of 30 mΩ for the HE type and 29 mΩ for the HP type, respectively. The similarity in the ohmic resistance implies that such a factor is not critical for determining rate capability in the tests.

3.2. The $ps\text{-OCV} = f(\text{SOC})$ curves

Fig. 2 shows the $ps\text{-OCV} = f(\text{SOC})$ curves for the HE and HP type of cell, respectively. Overall, the shape of two curves are similar and display the profile of a classic GIC||LFP cell with well-marked plateaus attributed to the five (labeled from ① to ⑤) staging reactions in the GIC from pure graphite to LiC_6 [23]. There are some

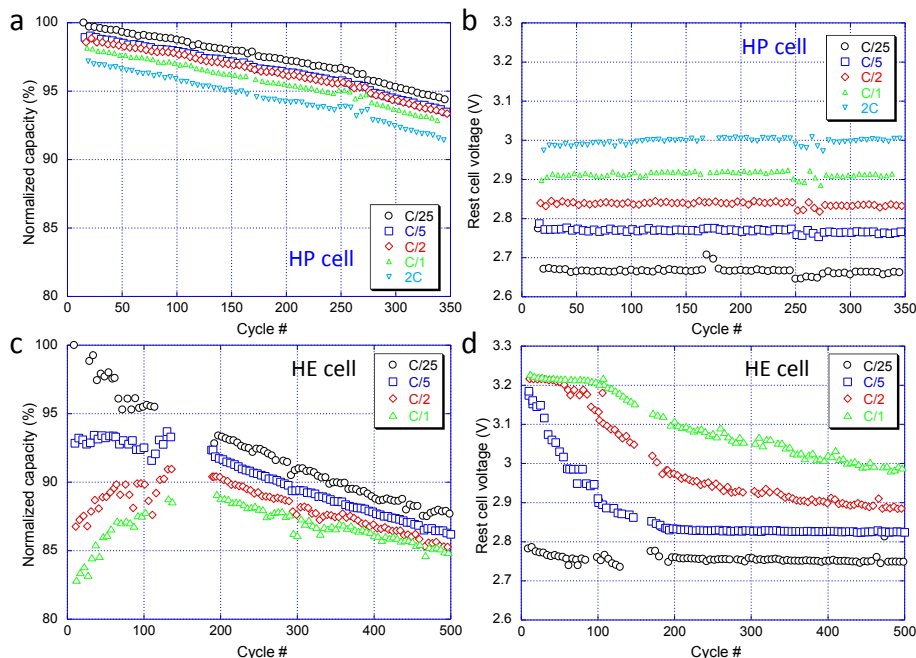


Fig. 4. Evolutions of (a) normalized capacity (against the cell maximum capacity) and (b) RCV, as a function of cycle number, in the HP cell; and, (c) and (d), *idem*, respectively, in the HE cell.

distinctions between the two, depicting the displacements in regions where the voltage varies between adjacent plateaus and the variations in the span of the plateaus against SOC. Elaboration on these subtle differences are described in Section 4.1.

3.3. Dependence of EOD RCV on rate

Fig. 3 presents the dependence of the RCV at the EOD (where the cutoff voltage was 2.5 V) as a function of rate in the HE and HP cells. In general, the lower the voltage is, the lower the SOC. The RCV has a stronger and more sensitive dependence with rate in the HE cell than in the HP cell. In contrast, such dependence is less sensitive in the HP cell until approaching very low rates below C/5. The RCV of the HE cell is consistently higher than that of the HP cell at all rates. At rates higher than 1 C, the EOD RCVs of the HE cell stay in a voltage plateau region. The HP cell was discharged to RCVs below 2.9 V at all rates, suggesting a better utilization of the active materials in the design (i.e. it can reach a lower SOC at the EOD than the HE cell does).

3.4. Aging behavior

Fig. 4 shows the evolution of normalized capacity and the RCV in each cell type with cycle number in the aging process. In the HP cell, the capacity faded linearly by 5% at the end of 300 cycles (i.e. fade rate = $0.017\% \text{ cycle}^{-1}$), as exhibited in Fig. 4(a). The fade rate appears independent of C rate, suggesting that the fade is not caused by any reaction kinetics degradation (RKD). This hypothesis is corroborated with additional evidence in polarization resistance (not shown) and the RCVs (Fig. 4(b)), since neither varies with cycle number. The HE cell exhibits a complicated fading pattern, as shown in Fig. 4(c), which is similar to the one observed in our previous work [9]. The capacity fade at C/25 is higher than that in the HP cell in the beginning of the cycle aging (i.e. 4% capacity fade in the first 80 cycles, or a fade rate = $0.050\% \text{ cycle}^{-1}$). The fade

occurred at a slower pace as cycle aging continued (e.g. additional 6% fade from cycle 200 to 500 or a fade rate = $0.020\% \text{ cycle}^{-1}$). In the case of C/5, the capacity appears relatively stable in the first 80 cycles; although the trend suggests that it subtly increases to a maximum around cycle 60 and then decreases at a pace of $0.018\% \text{ cycle}^{-1}$ (or 5.5% capacity fade from cycle 200 to 500). At C/2 and 1 C, the capacity increased with initial cycle aging in a more distinctive manner, by 3% and 5% in the first 100 and 130 cycles to reach a maximum, respectively. The capacity subsequently decreased at $0.015\% \text{ cycle}^{-1}$ and $0.013\% \text{ cycle}^{-1}$ to the end of 500 cycles, respectively. In the last 300 cycles, the capacity fade rate is similar to that of the HP cell for all C rates.

The evolution of the RCVs with cycle number in the HE cell is complicated as well, as shown in Fig. 4(d). At C/25, the RCV decreased slightly from 2.80 V to 2.75 V in the first 80 cycles and stayed at 2.75 V to the end of 500 cycles. At C/5, the RCV decreased from 3.20 V to 2.82 V in the first 200 cycles and remained at 2.82 V to the end of 500 cycles. At C/2 and 1C, the RCV was rather stable above 3.20 V (on a voltage plateau) for the first 60 and 100 cycles, followed by a gradual decrease to 2.90 V and 3.00 V, respectively, at the end of 500 cycles. The initial and ending RCV values in the first 500 cycles are close to those observed in Ref. [9], indicating the experiments successfully reproduced the capacity fade results and the evolutions of RCV for several rates in the first 150 cycles of aging of our previous work.

Fig. 5(a) shows the evolution of the cell voltage right after the initial IR-drop (V_{IR}) in the HE cell with cycle number for C/25, C/5, C/2 and 1C. In the first 150 cycles, the V_{IR} remains the same at C/25. At C/5 and above, the V_{IR} increases with cycle number and the variation is rate dependent in a linear fashion (Fig. 5(b)). The increasing V_{IR} suggests the apparent ohmic resistance of the cell decreased with cycle number (by 25% in the first 150 cycles), while the capacity increased with cycle number at these rates. The increase in capacity was a function of C rate as well. The V_{IR} was rather constant for the HP cell at all rates in the entire 350 cycles (not shown).

4. Discussion

4.1. Performance variations between HP and HE cells

The results from Fig. 1 suggest the significant difference in rate capability between the two types does not hinge on form factor or cell resistance. Fig. 2 indicates that the $ps\text{-OCV} = f(\text{SOC})$ correspondence in each cell depends on the NEAM and PEAM loading in the electrodes, and each design has a specific loading ratio ($LR = Q_{NE}/Q_{PE}$) [10]. Fig. 3 indicates that the utilization of active materials in the HE cell is much less extensive than in the HP cell at the same rate, since the EOD RCV shows that the SOC of the HP cell is lower than that of the HE cell at the EOD of each comparable rate. Therefore, the rate capability difference as depicted by the Peukert plot in Fig. 1 is likely due to the mass transfer differences between the two cell designs. These differences introduced by the cell design should include the effects caused by the electrode architecture, the LR and loading matching between the two electrodes (i.e. the actual range of composition used in the cell reaction in the PE and NE respectively, and an offset in the loading matching (OFS) as a result of the initial SEI formation). One should be mindful that these effects would also change as the cell ages. The variations in the LR and OFS could change the thermodynamic property of a cell (e.g. the chemical compositions and their equilibria), as depicted by the $ps\text{-OCV} = f(\text{SOC})$ curve [10]. Such subtle variations explain the differences between the $ps\text{-OCV} = f(\text{SOC})$ curves in the HP and HE designs.

The first distinction in the differences is the length of plateau ① (which represents the extent in the phase transformation from LiC_6 to LiC_{12} in the cell [23]), which suggests that the transition from ① to

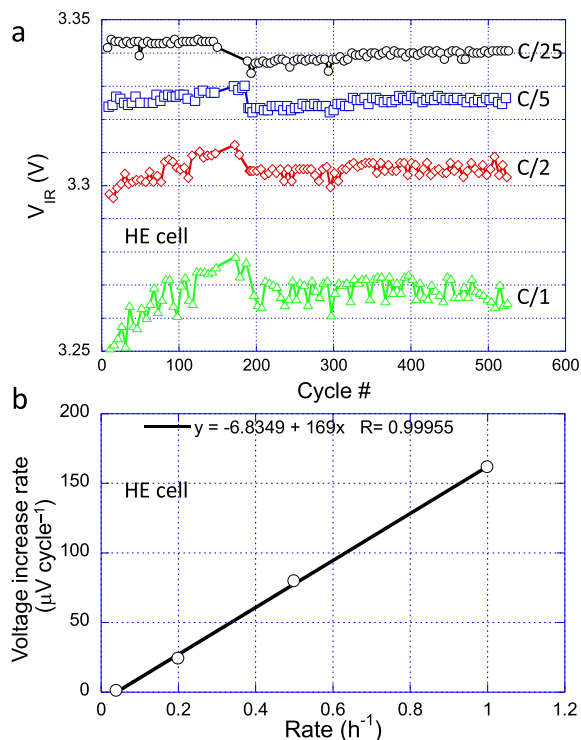


Fig. 5. (a) Evolutions of V_{IR} as a function of cycle number and (b) rate of voltage increase as a function of discharge rate in the HE cell.

● occurs at a higher SOC in the HP than in the HE cell (Fig. 2). A shorter plateau ● implies that the NE is less lithiated at the EOC. Thus, assuming the same quantity of Li from the PEAM (i.e. LFP) was involved in the charging process, there must be more NEAM (graphite) used in the reaction in the HP cell. In other words, a higher LR must exist in the HP cell than in the HE cell. Section 4.2 presents a more detailed explanation on how to determine LR in the model.

The second distinction in the two $ps\text{-OCV} = f(\text{SOC})$ curves is the shape of the curve in the region beyond plateau ● where SOC is less than 10%. In this last portion of the curve, the voltage descends more rapidly in the HE cell. This is also a result of the difference in the LR between the two cells since a higher LR leads to a longer voltage plateau ●. The higher LR in the HP cell makes the discharge curve appears longer in the plateau regions and more gradual in the transition from one plateau to the adjacent one.

In the HP cell, the RCVs are all below the 3.20 V plateau (i.e. plateau ● in Fig. 2) at the EOD, which suggests that at least the NE was almost fully delithiated to its maximum extent at all C rates [1,10]. In contrast, in the HE cell, the RCVs are on the 3.20 V plateau at 1 C and 2 C, implying that the PE is much less discharged (lithiated) at the EOD. This 3.20 V plateau is still well defined above 2 C in a Li||GIC half-cell [10], which suggests that the NE should be able to handle rates up to 2 C. This postulation thus implies that the disparity in the EOD RCV versus rate correspondence in the two cells, as shown in Fig. 3, is a result of the retarded rate capability in the PE, likely due to the electrode architecture that constrains the delivery of capacity. Up to 2 C, the LFP in the HP cell is highly utilized and lithiated to yield a lower SOC and RCV than in the HE cell. It is known that a HP cell tends to utilize a thinner electrode design with a higher porosity and less loading than a HE one, optimized for power capability, not capacity.

4.2. Simulation of cell performance by the 'Alawa toolbox'

The 'Alawa toolbox provides a convenient graphical user interface allowing users to perform simulation of cell performance by selecting PEAM and NEAM, LR, OFS, and C/n rate. The first step in

the simulation is to determine the composition of the HP and HE cells, respectively, to emulate their performance characteristics as a function of rate. Two variables, LR and OFS, are critical in obtaining accurate emulation results agreeing with test data. To achieve this, we rely on accurate emulation of the $ps\text{-OCV} = f(\text{SOC})$ curve for each cell design [10]. Fig. 6(a) shows an emulated $ps\text{-OCV} = f(\text{SOC})$ curve of a GIC||LFP cell with LR = 1.1 and OFS = 9%. LR and OFS are actually coupled, which can be expressed as $\text{LR} = f(\text{OFS})$. To yield a good estimate of LR and OFS for a cell, one can examine the capacity of the composition range associated with plateaus ●–● ($Q_{\bullet-\bullet}$). This composition range of plateaus ●–● corresponds to the phase transformations from LiC_{12} to C; thus, $Q_{\bullet-\bullet}$ shall account for half of Q_{NE} [23]:

$$Q_{\text{NE}} = 2Q_{\bullet-\bullet} \quad (1)$$

By definition, $\text{LR} = Q_{\text{NE}}/Q_{\text{PE}}$; but, unfortunately Q_{PE} could not be determined directly from experiments. The only capacity can be determined with sufficient accuracy is Q , that of the full cell. Nonetheless, Q_{PE} can be expressed as a function of Q and OFS, following the illustration in Fig. 6(a):

$$Q_{\text{PE}} = Q + \text{OFS} \times Q_{\text{PE}} = \frac{Q}{1 - \text{OFS}} \quad (2)$$

where OFS is typically scaled as a percentage of Q_{PE} . From Equations (1) and (2), the LR can then be expressed as a function of OFS, Q_{NE} and Q :

$$\text{LR} = \frac{Q_{\text{NE}}}{Q_{\text{PE}}} = \frac{(1 - \text{OFS})Q_{\text{NE}}}{Q} \quad (3)$$

From Fig. 2 we can estimate that $Q_{\bullet-\bullet}$ accounts for 70% of Q in the HP cell, and 60% in the HE cell. According to Equation (1), Q_{NE} in each cell can then be estimated. Thus, it is 140% of Q in the HP cell and 120% in the HE cell. Equation (3) can now be used to estimate $\text{LR} = f(\text{OFS})$, as shown in Fig. 6(b). Following Equation (3), the LR could vary between 1.0 and 1.4, while the OFS varies between –17% and 30%.

In principle, one could estimate the best couple of (LR, OFS) for each cell by going through a series of iteration of (LR, OFS) to generate an IC curve that represents the best fit with the experimental data. For LFP-based chemistry, this process is challenging, since LFP exhibits a voltage plateau, and all the IC curves with different (LR, OFS) values shall exhibit a very similar shape. However, more distinctive variations can be detected by examining the shape of the IC peaks of ● and ● near each end of the curve, since in these areas the variations are more sensitive to the loading matching, which should allow a proper determination of the best (LR, OFS) couple. In this work, the half-cell data used in the model however do not correspond to the actual active materials used in the cells. The electrode microstructure and morphology might also affect the transport kinetics. Therefore, the simulated peak shape for peaks ● and ● does not match closely with the experimental data. Thus, it is impossible to determine the actual values of the OFS and LR for the test cells in this case. Nonetheless, it is known that the irreversible capacity loss during formation cycles is typically in the range of 10–15%. Thus, it is reasonable to assume OFS around 10%; and therefore, LR = 1.1 and 1.25 were chosen for the HE and HP cell, respectively, in this study. It is worth mentioning that using OFS = 15% does not change the results of the discussion. The LR and OFS values for a pristine cell upon the completion of the initial formation process or conditioning and before the cycle aging are denoted as LR_{ini} and OFS_{ini} , respectively.

Another issue encountered in the simulation is the availability of the half-cell data for the HE cell. The LFP half-cell data used in the

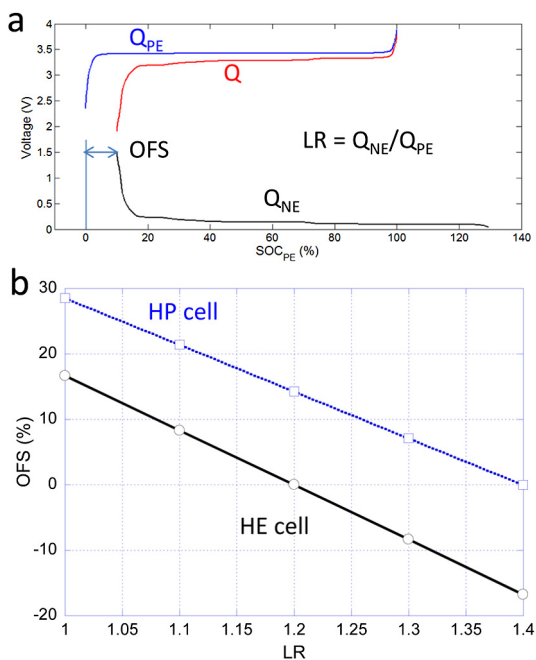


Fig. 6. (a) A schematic showing how an emulated $\text{OCV} = f(\text{SOC})$ curve of a GIC||LFP cell was derived and (b) the correspondence of OFS and LR in the HP and HE cells derived from Equation (3).

model is from an HP cell. Modification of this data for the HE cell is thus necessary. This was achieved by rescaling the charge and discharge curves of the half-cell data to agree with the capacity at each rate as expected from the experimental Peukert curve of the HE cell.

Despite the fact that the PEAM and NEAM used in generating the half-cell data might not be the same as those used in the actual test cells, we are confident that the trends and results derived from this work are relevant, which should provide sufficient fidelity to explain the phenomena studied in this work.

4.3. Degradation mechanism

The peculiar differences in the aging behavior between the HP and HE cells, as shown in Figs. 4 and 5, require a better understanding of the degradation modes to explain these intricate results. To help the understanding of the degradation modes underpinning the capacity fading in both cells, mechanistic simulation using the 'Alawa toolbox based on the model reported in Ref. [10] was used along with the incremental capacity (IC or $dQ/dV = f(V)$) analysis. The experimental data analysis and simulation should provide a more insightful description of the cycle aging and degradation phenomena to explain the differences between the two cell types.

Possible capacity fading modes in the GIC||LFP cells have been studied and discussed in the literature [1–9]. In general, the capacity fade in a HP cell is mainly attributed to loss of lithium inventory (LLI). However, loss of active material (LAM) should not be excluded either, because it often shows up as the dominant mode towards the end of life. LAMs can occur in the PE (LAM_{PE}) or the NE (LAM_{NE}) in either lithiated (li) or delithiated (de) state. Therefore, there are five possible degradation modes that could contribute to the capacity fade (i.e. LLI, LAM_{liPE} , LAM_{dePE} , LAM_{liNE} , and LAM_{deNE}). Using the 'Alawa toolbox and the modeling approach in Ref. [10], it is plausible to study various scenarios of degradation via simulations; e.g. how the capacity fades during cycle aging; how much fade each mode contributes to the total capacity loss; or, how the aging symptoms in the cell performance, such as the cell voltage variations, displayed with rate or cycle number in the cycle aging.

4.3.1. High-power cell

In the HP cell, 5% fades were measured after 300 cycles in the C/25 and C/5 discharge regimes, with a linear fade rate of $0.017\% \text{ cycle}^{-1}$, independent of C rate. To understand this aging behavior, we began with the case of C/25, and the modeling using the 'Alawa toolbox was used to simulate a series of hypothetical scenarios of capacity fading from each degradation mode individually. Equations (4) and (5) denote how LR and OFS were calculated and used in the model for each single degradation mode, respectively:

$$LR = LR_{ini} \left(\frac{100\% - \%LAM_{deNE} - \%LAM_{liNE}}{100\% - \%LAM_{dePE} - \%LAM_{liPE}} \right) \quad (4)$$

$$OFS = OFS_{ini} + LR \times \%LAM_{liNE} - \frac{LR}{LR_{ini}} \times \%LAM_{dePE} + \%LLI \quad (5)$$

As each parameter was treated with a progressive contribution in $\%LAM$ or $\%LLI$ as a function of cycle number, commensurate with the fade rate, from each degradation mode, the resulting $ps\text{-OCV} = f(\text{SOC})$ curve as a function of cycle number was simulated for each single degradation mode. The cutoff conditions and rate for the cycle aging were further applied in the simulation to obtain the capacity variations as a function of cycle number in each mode, as shown in Fig. 7(a) and (b) for C/25 and C/5 respectively. Through the

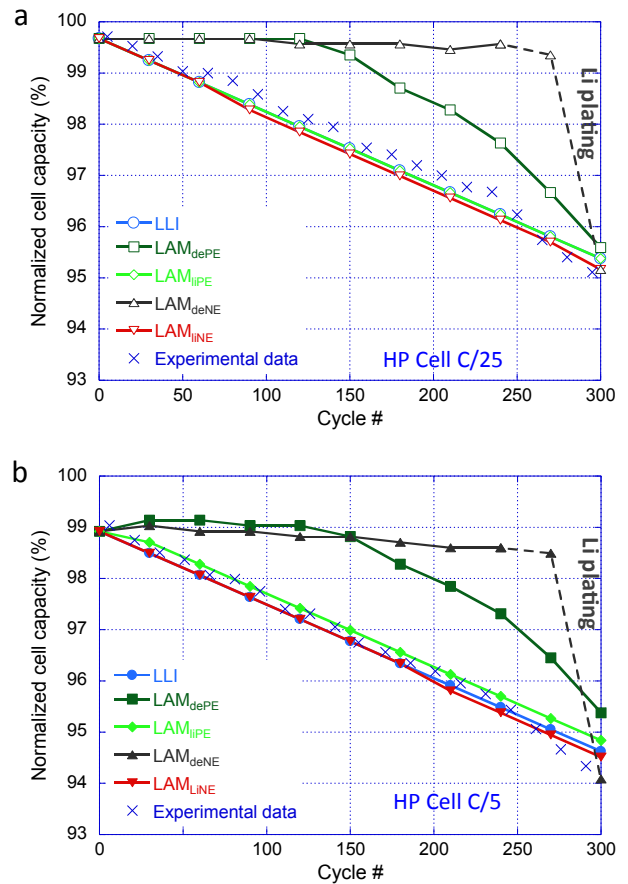


Fig. 7. Trends in capacity fading as a function of cycle number for the five degradation modes: 4.5% LLI, 4.5% LAM_{liPE} , 16.5% LAM_{dePE} , 27.0% LAM_{deNE} , and 4.0% LAM_{liNE} , respectively, as predicted for (a) C/25 and (b) C/5, in comparison with test data. All simulations are based on 5% capacity fade in a HP cell using the 'Alawa model reported in Ref. [10].

comparison with the experimental data, the simulation results can be used to decipher the fading mechanism. Those who are interested in this aspect should refer to the discussion provided in Ref. [10]. In the case of LAM_{deNE} , additional side effect should be considered should the NE become limiting in the charge regime, where Li plating could occur. Such an effect was not observed in this work. More details on the aspect of Li plating issues in the model should be referred to the discussions in Ref. [10] or a broader discussion in Ref. [24].

In Fig. 7(a), each of the following cases: 4.5% LLI, 4.5% LAM_{liPE} , 16.5% LAM_{dePE} , 27.0% LAM_{deNE} , or 4.0% LAM_{liNE} , shall give 5% capacity fade in the cell. In each case of simulation for a single degradation mode, the contributions from other modes were assumed negligible in Equations (4) and (5). Compared to the experimental results, three degradation modes: LLI, LAM_{liPE} and LAM_{liNE} , conformed to the trend line described by the capacity variations as a function of cycle number. LAM_{dePE} and LAM_{deNE} were thus excluded as plausible attributes for the capacity loss, since the predicted trend lines are quite different from that of the test results. The simulations at C/5 (Fig. 7(b)) could not provide any additional information to resolve among LLI, LAM_{liPE} and LAM_{liNE} either.

We thus resorted to IC (or dQ/dV) analysis to seek resolution. Since the three degradation modes should alter the LR and loading matching relationship between the two electrodes to different degrees [10], the analysis might help deciphering which is the cause for the fade. Fig. 8(a) presents the simulated IC curves at C/25

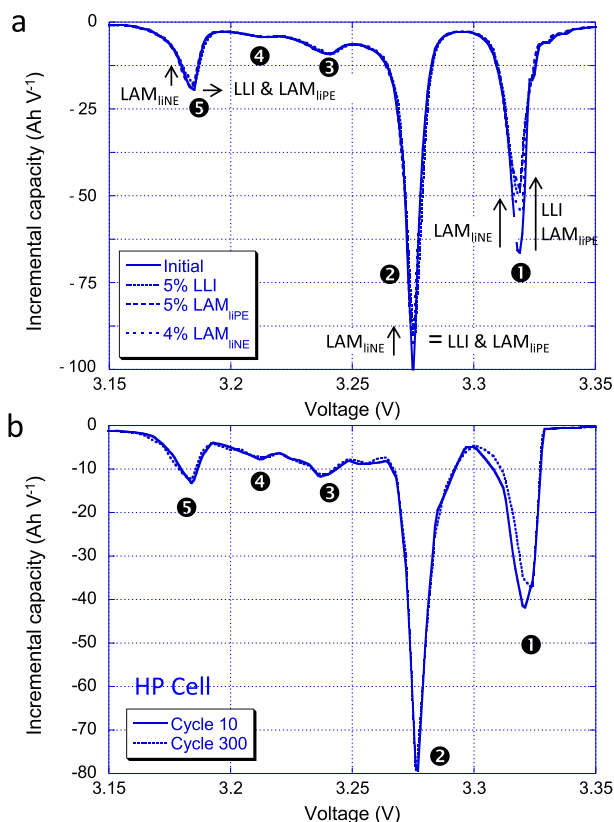


Fig. 8. (a) Simulated IC (dQ/dV) curves at C/25 for 5% LLI, 5% LAM_{IPE} , and 4% LAM_{IINE} in comparison with that of the cell without aging. Arrow (e.g. \rightarrow) and equal ($=$) signs are used to indicate the changes from the virgin curve to those with degradation. (b) Experimental IC curves of the HP cell at cycle 10 and cycle 300 to exhibit the deviations from the capacity fade.

for the cases of 5% LLI, 5% LAM_{IPE} , and 4% LAM_{IINE} . The simulation suggests that LLI and LAM_{IPE} conformed to the test result, but LAM_{IINE} did not. It is however difficult to decipher between LLI and LAM_{IPE} with sufficient confidence, since the two coincide with each other in the capacity fade trend curves and fade-associated symptoms (e.g. the intensity of peak 1 is supposed to be reduced, while that of peak 2 remains practically unchanged; and, the position of peak 5 is supposed to shift toward a higher voltage). In the case of LAM_{IINE} , all IC peaks were supposed to decrease in intensity or peak area, according to the simulation.

Fig. 8(b) exhibits the IC curves of the HP cell at cycles 10 and 350 from the test. As the HP cell aged to cycle 350, the intensity of peak 1 decreased, yet all other peaks appeared unchanged. This result eliminates LAM_{IINE} as a plausible cause. However, the IC analysis cannot resolve the remaining two. It is difficult to tell if the resolution of the tester might be able to.

To resolve which of the two (LLI and LAM_{IPE}) might be the cause, we next looked into the characteristics abided by the nature of each mode for distinction. One of these aspects is V_{IR} . LLI is supposed to lose usable Li ions to parasitic reactions, leading to byproducts in the electrolyte solution or on the electrode surface; but it should not change the content of the active materials in the electrodes and their properties, such as the ohmic resistance (which primarily consists of the electrolyte conductance and the resistance related to the electronic pathway in the electrode matrix) in a noticeable manner. Thus, the LLI is not expected to affect V_{IR} . In contrast, LAM_{IPE} shall reduce the LFP loading in the PE and, in turn, increase the actual C rate on the PE. As such, we would expect that LAM_{IPE} affect the V_{IR} more noticeably than LLI. Since the V_{IR} stayed within a stable range in the cycle aging even at 2 C, we are thus inclined to believe that the capacity fade is likely a result of LLI, less likely of LAM_{IPE} . This conclusion is consistent with the view in the literature.

4.3.2. High-energy cell

The same capacity fading analysis was performed for the HE cell. Fig. 9(a) shows the simulation results for C/25 capacity fade in the

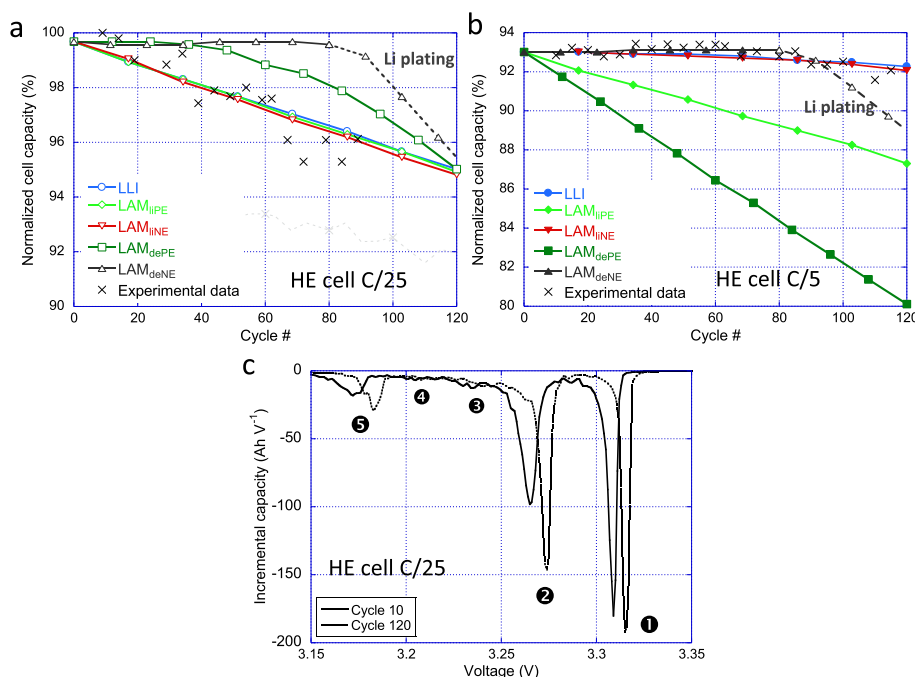


Fig. 9. Capacity fading trend predictions for a HE cell at (a) C/25 and (b) C/5 based on 10% capacity fade, according to the 'Alawa model' [10] simulations, and (c) the experimental IC curves of the HE cell under C/25 discharges at cycles 10 and 120.

first 120 cycles. It is possible to attribute to the observed 6% fade at C/25 from 5.5% LLI, 5.5% LAM_{LiPE}, 17.0% LAM_{dePE}, 15% LAM_{deNE} or 5.0% LAM_{LiNE}, respectively. Analogous to the analysis of the HP cell, LLI, LAM_{LiPE} and LAM_{LiNE} conformed to the observed fading trend at C/25. However, the C/5 capacity fading simulations were able to discriminate LAM_{LiPE} due to inconformity to the observed fading trend line in Fig. 9(b).

The following IC analysis was applied next to seek a resolution between the remaining two, LLI and LAM_{LiNE}. Fig. 9(c) shows the IC curves of the HE cell at C/25 in the initial stage of aging at cycles 10 and 120. The IC curves exhibit a surprisingly different pattern of behavior in contrast to those of Fig. 8(b). All IC peaks become sharper (i.e. with an increased intensity and narrowed peak half-width) and all peak positions shift to higher voltages as the cell aged from cycle 10 to 120. It should be noted that an IC peak intensity variation alone is not a definitive piece of evidence for deciphering degradation modes. Additional evidence is often required to validate the attributes with sufficient confidence. Here, we shall consider the integral peak area in the IC curve and distribution among distinct IC peaks to derive additional information for examination. The integral peak area and its distribution with IC peaks in an IC curve depict the capacity variations commensurate with the flux and extent of the underlying electrochemical reaction; thus, without a fade, the integral peak area should be invariant to the shape of the curve. Even if the shape of the IC curve might vary with aging, the integral peak area might not so long as there is no fade involved. On the other hand, if a fade occurred, not only the shape could vary, but also the peak area associated with a specific IC peak might change with the fade, which in turn should provide insightful information about the mechanism. For instance, in Fig. 8(a), were LLI the underlying mode for the fade, the integral area of peak ① should decrease in a noticeable manner, whereas the shape and the integral area of peaks ②–⑤ should not. On the contrary, were LAM_{LiNE} the cause, the integral area of peaks ②–⑤ is supposed to decrease.

Fig. 10 presents the evolution of the normalized integral areas of (a) peak ① and (b) peaks ②–⑤ as a function of cycle number at C/25 in the first 120 cycles of aging. The experimental data are compared with those predicted by 'Alawa' model for single modes based on 5.5% LLI and 5.0% LAM_{LiNE}, respectively. The results showed that the area of peak ① decreased linearly at a pace of $-0.1\% \text{ cycle}^{-1}$ and that of peaks ②–⑤ at $-0.05\% \text{ cycle}^{-1}$. Neither mode could conform to both experimental trend lines, indicating that the capacity fade does not attribute to any of them alone. The results depicted that the area of peaks ②–⑤ decreased faster than those predicted from LLI and LAM_{LiNE}, respectively, whereas of peak ① at a pace between the two predicted. Such a complicated result in the correspondence of peak area in different regions of the IC curve suggests that the fading may have involved a combination of degradation modes

with different specific paces in the aging. Any simple discrimination of individual degradation modes in the deciphering of the aging behavior does not seem to work well here.

To understand these complicated results in the HE cell aging in order to aid us determine the underpinning mechanism, we shall invoke a broader range of considerations on a few possible scenarios. We shall begin with the case of C/25 (Fig. 9(a)), assuming that the kinetic contributions would be relatively negligible to simplify the analysis. Furthermore, we shall not discriminate LAM_{dePE} and LAM_{deNE}, as we practiced by simple eliminations before. On the contrary, we shall figure what role they could play in the fading. The 'Alawa' simulation results suggest that LAM_{dePE} or LAM_{deNE} should not exhibit any fade initially until the cell reaches a massive capacity fade in the cycle aging. Under severe LAM_{deNE}, Li plating could be expected. The extent of LAM_{dePE} or LAM_{deNE} without the presence of measurable capacity fade should depend on the cell design, including LR and loading matching. Furthermore, LAM_{dePE} or LAM_{deNE} should induce changes in LR and loading matching, leading to alterations of the $ps\text{-OCV} = f(\text{SOC})$ curve and the associated IC curve. Such alterations in IC curve could be useful clues for us to identify degradation mode. The propensity of having LAM_{dePE} or LAM_{deNE} without a measurable fade also prompts us to consider and postulate that capacity fade could come from contributions of a predominant mode accompanied with an array of possible subsidiary modes; some might be much less prominent or 'hidden' (such as in the case of LAM_{dePE} or LAM_{deNE}).

The 'Alawa' simulations revealed that LAM_{dePE} could lead to a rapid capacity fade at C/5 (Fig. 9(b)), which is clearly against the experimental results. Therefore, the likelihood of having LAM_{dePE} involved in the fade is quite slim. The LAM_{deNE} mode, on the other hand, may introduce a significant alteration on the IC curve at C/25. Intriguingly, it could cause a decrease in the integral area of peaks ②–⑤, but come with a balanced increase in the integral area of peak ①, to maintain the overall peak area constant. As shown by the results in Fig. 10(a) and (b), a combination of 5.5% LLI and 5% LAM_{deNE} is close to the best fit of the observed fading behavior in the peak integral area evolutions of the IC curve. A couple of other combinations are worth noting for comparison. The combination of LAM_{LiNE} and LAM_{deNE} could also decrease the area of peaks ②–⑤ sufficiently to conform to the result in Fig. 10(b). However, it would then overestimate the increase in the area of peak ①, failing to reach a conformable result with the data in Fig. 10(a). The combination of LLI and LAM_{LiNE} could reduce the area of peaks ②–⑤ as well, but it led to a retarded decrease in the area of peak ①, also failed to conform to the experimental data.

The aging phenomenon in the last 300 cycles (from cycle 200–500) in the HE cell is investigated subsequently. Fig. 11(a) shows the peak area variations of peaks ②–⑤ and peak ①, respectively, as a function of cycle number from cycle 200 to 500, where the results

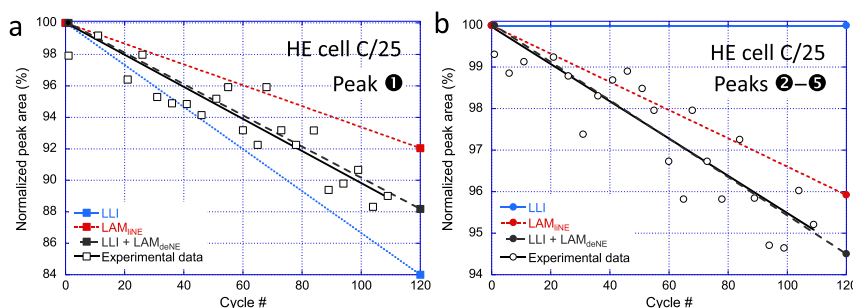


Fig. 10. (a) Normalized peak area for peak ① (□) and (b) *idem* for peaks ②–⑤ (○) as a function of cycle number in the first 120 cycles of aging in the HE cell. The experimental data are in symbols and solid lines, while the simulated results are in dotted or dashed lines. The simulated results are exhibited for LLI, LAM_{LiNE}, and LLI + LAM_{deNE}, respectively.

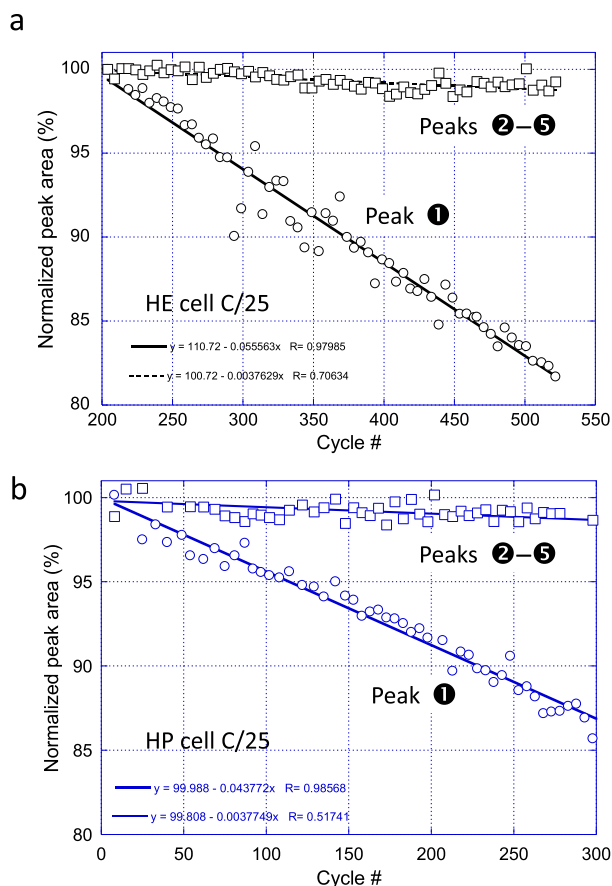


Fig. 11. Integral area variations of peaks 1 and 2–5 as a function of cycle number in (a) the HE cell in the last 300 cycles of aging and (b) the HP cell in the first 300 cycles of aging. In each plot, the symbols are: \square – experimental data for the integral area of peaks 2–5; \circ – *idem* of peak 1; and lines – simulated integral area variations with cycle number for peaks 1 and 2–5, respectively.

of cycle 204 were used as the baseline (100%) for comparisons. The variations of the peak area suggest that LLI is causing the capacity fade in the HE cell for cycles 200–500, as evident by the simulated peak area variation as a function of cycle number of this mode, that coincides well with the experimental data. The simulation also showed that the integral area of peaks 2–5 decreased by about 1%, suggesting that a minute degree of LAM_{deNE} likely occurred. It is not clear though why the initial attribute from LAM_{deNE} , which was comparable to the magnitude of LLI, becomes much less at this stage. When applying the peak area analysis to the HP cell, as shown in Fig. 11(b), the peak area variations from a combination of 5% LLI + 1% LAM_{deNE} is in excellent agreement with the test data, suggesting that the degradation mechanism in the HP cell is about the same as that in the HE cell from cycle 200 to 500. Since the trend of capacity fading is almost independent of cell design, it implies that this ‘LLI + LAM_{deNE} ’ fading mechanism is probably common in the LFP cell chemistry (with carbonaceous NE particularly) with LLI as the predominant mode in the degradation and accompanied with a less degree of LAM_{deNE} , which might be induced by LLI itself.

In summary, the degradation mechanism for the HE cell aging, as we have analyzed so far, comprises the following aspects: (1) In the analysis of the variations in capacity fade with cycle number, as shown in Figs. 4(c) and 9(a), we found that there are two possible modes, 5.5% LLI or 5.0% LAM_{LINE} , that could contribute to the 6% capacity fade. However, from the ‘Alawa’ simulation on each mode,

we could not discriminate between the two. (2) In the analysis of the integral area variations of peak 1 and peaks 2–5, as shown in Fig. 10(a) and (b), we found that the combination of 5.5% LLI + 5% LAM_{deNE} could explain the variations with sufficient accuracy for the fading behavior in the first 120 cycles of aging. Indirectly, we could neglect LAM_{LINE} in the consideration. (3) In the analysis of the subsequent cycle aging from cycle 200 to 500, additional 6% capacity fade was measured, and the primary mode was LLI, as evident from the ‘Alawa’ model simulations based on both the fade and the peak area variations. (4) Although the reduction in the integral area of peaks 2–5 was rather negligible, arguably about 1% in these 300 cycles (see Fig. 11(a)), we could not rule out LAM_{deNE} as an attribute to the degradation. (5) LAM_{IPE} was excluded from consideration because V_{IR} has been stable from cycle 200 to 500 (as indicated in Fig. 5(a)). (6) LAM_{dePE} was also excluded by its contradicting results with C/5 fading behavior. (7) The analysis shown in Fig. 11(b) suggests that LLI and a minute degree of LAM_{deNE} , about $0.003\% \text{ cycle}^{-1}$, was attributed to the capacity fade through the entire 300 cycles of aging in the HP cell, similar to the degradation in the HE cell during the second stage of aging from cycle 200 to 500.

4.4. Peculiar initial capacity increase with cycle aging in the HE cell

During the first 120 cycles of aging in the HE cell, the evolution of capacity fade at C/25 and C/5 (Fig. 4(c)) were attributed to a combination of LLI and LAM_{deNE} . However, the following phenomena in the HE cell aging remain unexplained and seem inconsistent with the expectations from the above fading mechanism, which invokes our desire to seek explanations:

- The LLI is taking place at a three-times-higher pace than that in the cycle 200–500 or in the HP cell,
- The LAM_{deNE} was unambiguously detected at a noticeable rate, and
- The capacity at rates higher than C/5 increase initially, which is counter-intuitive to what would be expected from the degradation mechanism.

In Fig. 9(c), it appears that even at C/25 the IC peaks became thinner and taller upon cycle aging. Another example is exhibited in Fig. 12, in which the evolution of peak 5 with cycle number at C/5 is presented. In the initial stage of cycle aging in the HE cell up to cycle 200 at C/25, the EOD RCV decreased gradually from 2.80 V to 2.75 V (Fig. 4(d)); likewise, at C/5, the EOD RCV decreased from 3.20 V to 2.82 V; thus, the reaction associated with peak 5 should be

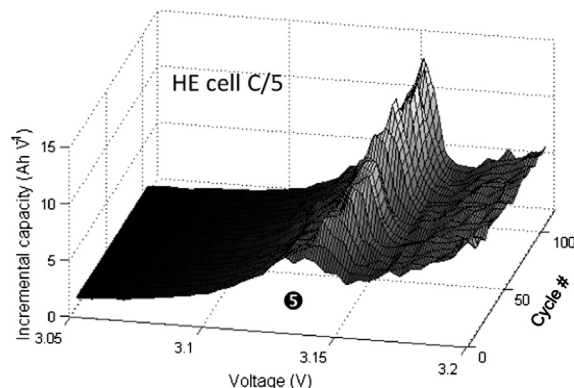


Fig. 12. Evolution of IC peak 5 at C/5 as a function of cycle number in the first 120 cycles.

considered complete in the test at C/25 or C/5. Peak ⑤ in the initial cycle aging period appeared very broad in shape. As cycle aging continued, the peak became thinner and more defined. In principle, the sharpness of the peak should reflect the cell kinetics of the underlying reaction at a specific rate. Therefore, as peak ⑤ becomes thinner and more defined in the cycle aging, the cell reaction kinetics must be improved. According to the half-cell data of the GIC, peak ⑤ is rather defined at C/5 versus a Li reference electrode. The width of peak ⑤ observed in the GIC||LFP cell is broader than that in the half-cell test. Hence, the broad peak exhibited by the HE cell is a sign of retarded kinetics at the PE that limits rate capability. As rate increases, the gradual increase in the capacity retention (Fig. 4(c)) and the decrease in the EOD RCV (Fig. 4(d)) during the initial cycle aging imply that improved kinetics and utilization of active material gradually become inherent to the PE.

It is useful here to comment on the EOD RCVs and their relationship with the terminal potential of each electrode in the LFP cell to derive a more comprehensive understanding of how aging accompanied with improved PE kinetics may affect cell performance. In general, disregarding the LR, the EOD cutoff at a certain rate shall be invoked by either the NE, when it is about to be delithiated fully, or the PE, when it is about to be lithiated completely. The test data could not provide this information unless a reference electrode is available. However, the RCV could provide some hints on the electrode composition, according to the electrode potential estimated in equilibrium. For instance, a RCV at 3.2 V shall imply the cell voltage is on a plateau in which both the PE and NE must be on a plateau potential, respectively. Especially, the NE must be in the staging phase transition region associated with peak ⑤.

In the HE cell, the C/25 capacity retention is predominantly controlled by the PE, and the kinetic effect is minimal. There is no 'reservoir effect' to mitigate LLI as the cell ages. Thus, the LLI shall undermine the capacity retention, as depicted in the fading trend in Fig. 4(c). The fact that the EOD RCV stays below 2.8 V in the aging suggests that the NE is close to be fully delithiated each time. Although a comparable amount of LAM_{deNE} (5% in the first 120 cycles) is occurring with LLI, the alteration in the LR does not affect the cutoff or the RCV in any noticeable manner. At C/5, the variation of the EOD RCV is quite noticeable, as it begins at 3.2 V but shortly runs into a descending path to reach a steady 2.82 V in the first 200 cycles. The RCV at 3.2 V indicates that the initial NE composition at cutoff must be on the peak ⑤ plateau. The subsequent descending of the RCV in the cycle aging suggests that the NE potential could not stay in the plateau anymore; instead, it is getting more delithiated each cycle, whereas the PE remains on its plateau. Improved PE kinetics shall mitigate the loss caused by LLI and LAM_{deNE} and aid the capacity retention in the initial 120 cycles of aging. At higher rates, both the PE and NE remain on the respective plateau at cutoff. Although LLI and LAM_{deNE} take place, the 'reservoir effect' shall mitigate any capacity loss. However, as the PE kinetics improves along with a lower polarization resistance, the PE potential shall be less polarized at the same SOC. Accordingly, the terminal NE potential shall be higher at the cutoff. A higher potential implies a more delithiated state in the NE; and, as more Li ions are exchanged, it shall lead to a better capacity retention and a lower RCV, which explains the results in Fig. 4(c) and (d). This reservoir effect has been previously discussed in Ref. [10].

Improvements of electrode kinetics in a manufactured cell could occur via the following mechanisms through cycle aging: (1) an improved percolation network for the electronic conduction in the electrode, (2) an improved mass transfer in the electrolyte in the porous electrode matrix, (3) an increase in the active surface area of the active material in the electrode; all due to possible electrode

morphology changes, and (4) an improved charge transfer kinetics at the electrode–electrolyte interface.

Were the fade rate = 0.017% cycle⁻¹ a nominal rate for LLI in the HP cell, the high fade rate = 0.050% cycle⁻¹ in the HE cell in the initial 120 cycles of aging is quite unusual. In a HP design, electrodes are usually thinner and contain more surface area per mAh and g of active material to provide better rate capability than in a HE design. As such, one would expect that the LLI fade rate should be higher in the HP cells than in the HE ones. In addition, such a high LLI fade rate was accompanied with a commensurate amount of LAM_{deNE} (Fig. 10(a) and (b)). The LAM_{deNE} mode seems diminished once the capacity retention at high rates stabilized, accompanied with steady polarization resistance (Figs. 5 and 11). It appears difficult to explain these phenomena simply by improved charge transfer kinetics (i.e. mechanism 4). Thus, it prompts us to consider changes in the electrode morphology or architecture as possible causes. Creation of cracks, microstructural defects are known in the literature for PE, as reported in stress modeling efforts for cells in a HE design [13] or by experimental results [14,15]. We shall characterize these phenomena as the results of an 'electrochemical milling' process. An immediate consequence from this process is an increase of the active surface area in the PE (mechanism 3), which could introduce subsidiary effects on improvements of electronic percolation network (mechanism 1) and mass transfer in the electrolyte due to improved tortuosity in the porous electrode matrix (mechanism 2). The integral improvement is a lower effective current density imposed on the active LFP grains per unit active surface area for the same C rate. According to Fig. 1, the capacity retention is very sensitive to the C rate in the HE cell (as exhibited by a high Peukert constant). Thus, lowering of the effective local current density at the PE should result in an enhanced capacity retention for the same C rate in the cycle aging. Furthermore, the electrochemical milling shall produce smaller grains in the PE, which allows shortened diffusion pathways for Li ions in the grains. However, recent models on Li intercalation in LFP [25] suggest that this effect should be minimal.

The electrochemical milling process may also introduce increased dissolution or leaching of Fe⁺³ ions or associated compounds into the electrolyte, which could migrate to the NE and poison the surface of the NE to increase SEI layer growth [26,27] or LLI. In a more severe situation, it might isolate some NE grains from the electronic or ionic percolation network. This explains not only a higher LLI fade rate but also the presence of a commensurate amount of LAM_{deNE} in the degradation. None of the LAM_{PEs} was detected in the experiments. However, the presence of electrochemical milling at the PE may not preclude the possibility that a noticeable amount of LFP grains might have been isolated from the electronic or ionic percolation network. The IC analyses as shown in Figs. 8(b) and 9(c) eliminate possible involvement of LAM_{LiPE}. However, it is difficult to tell if a small amount of LAM_{dePE} were present. An insignificant presence of LAM_{dePE} would not contribute to any discernible capacity fade. Worse than that, because the LFP PE exhibits an invariant voltage plateau during aging, degradation hardly will change this plateau voltage. LAM_{PE} shall only change the length of the plateau span, or the LR. As such, 'Alawa' simulations showed that any LAM_{dePE} that is less than 10% will be difficult to detect or quantify for capacity fade, as evident by the experimental data with rates up to 2 C.

The extent of the electrochemical milling is estimated from Fig. 5(a) and the changes in the apparent polarization resistance in particular. Since V_{IR} is rate dependent, the slope of the $V_{IR} = f(I)$ curve corresponds to the cell apparent polarization resistance. Fig. 13 presents the V_{IR} as a function of rate at cycle 10 and cycle 150. The slope of the curve has been decreased from cycle 10 to 150, thus the apparent polarization resistance decreased. This is another

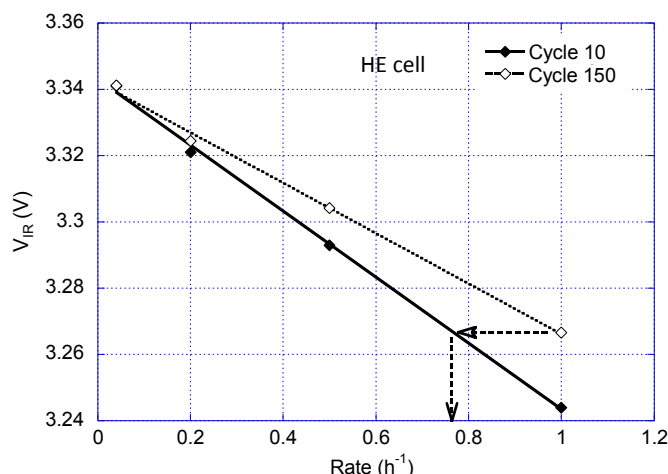


Fig. 13. V_{IR} as a function of rate at cycle 10 and 150 in the HE cell.

piece of indirect evidence derived from the changes in the active surface area with initial cycle aging in the presence of electrochemical milling. The increase in the active surface area lowers the effective local current density at the PE, as exhibited by the smaller polarization and lower polarization resistance at a given C rate.

The following assumptions are useful for the estimation of the extent of changes in the active surface area by the electrochemical milling: (a) given that the improved electronic (mechanism 1) or ionic (mechanism 2) percolations might be apparent in the explanation, the impact on the magnitude of the polarization resistance might be negligible (e.g. at best, probably comparable to those in the HP cell). It is because such enhancements only create more parallel paths to increase percolation probabilities. They are not supposed to change the electronic or ionic conductivity substantially. Thus, they should not affect the polarization resistance in a significant manner. (b) The benefits of these enhancements might be countered and compromised by the increased SEI growth and the associated increase in polarization resistance. (c) On the contrary, the changes in the active surface area have more direct impacts on the polarization, since they change the effective current density on a local scale directly. The 25% decrease in the apparent polarization resistance (Fig. 5) must thus come from the change in the effective current density. In Fig. 13, the V_{IR} of 1 C rate at cycle 150 is the same as that of 0.75 C at cycle 10. Therefore, at the PE as the electrochemical milling continues to alter the electrode morphology, the current density at 1C in the beginning of life has transformed to a level equivalent to 0.75 C at cycle 150. If the active surface area increase at the PEAM were indeed the cause of such a variation, the active surface area can be estimated from the equivalent C rate, which is in proportion to the value of the applied current (based on the initial C rate) divided by the current density. Since the current density is lowered by 25%, the active surface area should thus increase by about 33% (i.e. $33\% = [(1/0.75) - 1] \times 100\%$).

5. Conclusion

The performance and cycle aging-caused degradation in two commercial GIC||LFP 26650 cells with HE and HP designs were studied here. The variations in performance between the two cell designs are explained by the differences in the electrode architecture, in terms of loading ratio and loading matching of the two electrodes; and the extent of reaction in the two electrodes under the test condition. These performance characteristics are simulated and predicted by a model reported in our prior work via a graphic

user interface, the 'Alawa toolbox. The degradation in capacity fade in these two cell designs are further analyzed and simulated using the IC (dQ/dV) techniques and the 'Alawa toolbox. Five degradation modes (i.e. LLI, LAM_{IjPE} , LAM_{dePE} , LAM_{IjNE} and LAM_{deNE}) were considered in the analyses and simulations to derive useful information for deciphering the underlying mechanism for capacity fade in each cell design. LLI was identified as the primary attribute to the capacity fade in the first 300 cycles of aging in the HP cell. The capacity fade in the HE cell is much more complicated. Besides analyzing and comparing the rate-dependent capacity fading and IC (dQ/dV) variations in HE cell degradation, IC peak area was also used as key information to determine the underpinning capacity-fading modes and quantify the amount of contribution from each mode. For the initial 120 cycles of aging, the 'Alawa model simulation indicates that a combination of 5.5% LLI + 5% LAM_{deNE} contributed to the initial 6% of capacity fade, based on the analysis of the IC peak area changes. From cycle 200 to 500, only LLI remains as the dominant mode for capacity fade. For the HP cell, similar analysis from the IC peak area changes suggests that a subsidiary contribution from LAM_{deNE} might also exist alongside the LLI. In the HE cell, a peculiar behavior related to the rate-dependent capacity variations in the initial 120 cycles of aging was attributed to the increase of the active surface area, on the order of 33%, produced on the PEAM by electrochemical milling. The consequences from this effect include (1) an abnormal high capacity fade rate on the order of 0.050% cycle⁻¹, compared to 0.017% cycle⁻¹ in the HP cell; (2) 5% capacity fades due to LAM_{deNE} , likely as a result of iron dissolution from the PE and subsequent impact on the NE that catalyzes additional SEI growth; (3) the gradual, rate-dependent increase of capacity at rates higher than C/5 during the initial cycle aging; and, (4) the gradual decrease in the EOD RCV, in association with the LLI.

It is useful to point out that the use of 'Alawa toolbox creates unprecedented benefits of this mechanistic approach to derive fading mechanism with quantitative comparisons for validation. The accuracy in the quantification, viability in comparing a large number of scenarios within a short time frame, the flexibility of comprising half-cell behavior into a full cell analysis, and the universality of combining multiple degradation modes in the model simulations (e.g. for both capacity and voltage variations as fading symptoms), all explicitly illustrate the benefits and merits of this approach to resolve complicated fading behavior in LIBs. The comparison of the HP and HE designs in a typical GIC||LFP cell exemplify this aspect perfectly.

Acknowledgments

The authors gratefully acknowledge funding provided by the Idaho National Laboratory under the Advanced Battery Research Program of the Office of Energy Efficiency and Renewable Energy of the United States Department of Energy (Contract No. DE-AC07-05ID14517). The authors are also grateful to Arnaud Devie for fruitful discussions and proofreading of the manuscript, Karim Zaghib of IREQ (Hydro-Quebec) for the LFP and Michael Spahr of TIMCAL for the GIC half-cell data.

References

- [1] M. Dubarry, B.Y. Liaw, M.-S. Chen, S.-S. Chyan, K.-C. Han, W.-T. Sie, S.-H. Wu, *J. Power Sources* 196 (2011) 3420–3425.
- [2] S.B. Peterson, J. Apt, J.F. Whitacre, *J. Power Sources* 195 (2010) 2385–2392.
- [3] N. Sharma, V.K. Peterson, M.M. Elcombe, M. Avdeev, A.J. Studer, N. Blagojevic, R. Yusoff, N. Kamarulzaman, *J. Power Sources* 195 (2010) 8258–8266.
- [4] J. Wang, P. Liu, J. Hicks-Garner, E. Sherman, S. Soukiazian, M. Verbrugge, H. Tataria, J. Musser, P. Finamore, *J. Power Sources* 196 (2011) 3942–3948.
- [5] Y. Zhang, C.-Y. Wang, X. Tang, *J. Power Sources* 196 (2011) 1513–1520.
- [6] P. Liu, J. Wang, J. Hicks-Garner, E. Sherman, S. Soukiazian, M. Verbrugge, H. Tataria, J. Musser, P. Finamore, *J. Electrochem. Soc.* 157 (2010) A499.

- [7] M. Safari, C. Delacourt, J. Electrochem. Soc. 158 (2011) A1123.
- [8] L. Castro, R. Dedryvère, J.B. Ledeuil, J. Bréger, C. Tessier, D. Gonbeau, J. Electrochem. Soc. 159 (2012) A357.
- [9] M. Dubarry, B.Y. Liaw, J. Power Sources 194 (2009) 541–549.
- [10] M. Dubarry, C. Truchot, B.Y. Liaw, J. Power Sources 219 (2012) 204–216.
- [11] R. Dominko, J.M. Goupil, M. Bele, M. Gaberscek, M. Remskar, D. Hanzel, J. Jamnik, J. Electrochem. Soc. 152 (2005) A858.
- [12] H. Huang, S.C. Yin, L.F. Nazar, Electrochem. Solid-State Lett. 4 (2001) A170.
- [13] J. Christensen, J. Electrochem. Soc. 157 (2010) A366.
- [14] H. Gabrisch, J. Wilcox, M.M. Doeff, Electrochem. Solid-State Lett. 11 (2008) A25.
- [15] D. Wang, X. Wu, Z. Wang, L. Chen, J. Power Sources 140 (2005) 125–128.
- [16] http://www.phostechlithium.com/prd_LiFePO4P1_e.php (accessed 06.01.14).
- [17] http://www.phostechlithium.com/prd_LiFePO4P2_e.php (accessed 06.01.14).
- [18] M. Dubarry, V. Svoboda, R. Hwu, B.Y. Liaw, Electrochem. Solid-State Lett. 9 (2006) A454–A457.
- [19] C. Truchot, M. Dubarry, B.Y. Liaw, Appl. Energy 119 (2014) 218–227.
- [20] M. Kassem, C. Delacourt, J. Power Sources 235 (2013) 159–171.
- [21] J.P. Schmidt, H.Y. Tran, J. Richter, E. Ivers-Tiffée, M. Wohlfahrt-Mehrens, J. Power Sources 239 (2013) 696–704.
- [22] M. Dubarry, C. Truchot, M. Cugnet, B.Y. Liaw, K. Gering, S. Sazhin, D. Jamison, C. Michelbacher, J. Power Sources 196 (2011) 10328–10335.
- [23] D. Aurbach, B. Markovsky, I. Weissman, E. Levi, Y. Ein-Eli, Electrochem. Acta 45 (1999) 67–86.
- [24] Z. Li, J. Huang, B.Y. Liaw, V. Metzler, J. Zhang, J. Power Sources 254 (2014) 168–182. <http://dx.doi.org/10.1016/j.jpowsour.2013.12.099>.
- [25] R. Malik, A. Abdellahi, G. Ceder, J. Electrochem. Soc. 160 (2013) A3179–A3197.
- [26] K. Striebel, J. Shim, A. Sierra, H. Yang, X. Song, R. Kostecki, K. McCarthy, J. Power Sources 146 (2005) 33–38.
- [27] H.-H. Chang, H.-C. Wu, N.-L. Wu, Electrochem. Commun. 10 (2008) 1823–1826.